

Article

Design and Validation of a Photoelectric Current Measuring Unit for Lunar Daytime Simulation Chamber

Seungsoo Park ^{1,*}, Taeil Chung ¹, Jihyun Kim ², Byunghyun Ryu ¹ and Hysoung Shin ¹

¹ Department of Future & Smart Construction Research, Korea Institute of Civil Engineering and Building Technology, 283 Goyang-daero, Ilsanseo-gu, Goyang 10223, Republic of Korea

² Wonik IPS Co., Ltd., 75 Jinwisandan-ro, Jinwi-myeon, Pyeongtaek 17709, Republic of Korea

* Correspondence: ssglenpark@kict.re.kr; Tel.: +82-31-910-0765

Abstract: Charging of the lunar surface induced by solar radiation can potentially threaten in situ resource utilization. Associated issues include dust adhesion and material degradation. Photoelectric currents are the primary cause of surface charging. This work reports on the development of a unit capable of measuring photoelectric currents in a vacuum chamber, which can simulate surface charging under conditions similar to those on the moon in daytime. The main components of the unit are a mesh grid, a photocathode specimen, and a ring collector. Photoelectric currents from an aluminum sample were measured by adjusting the electric potential of these components, and the impact of the electric potential of each component is discussed. Calculating the expected electric current within the experimental setup allowed validation of the current measurements: the measured and calculated values agreed well with an error of ~5.5%. Finally, the photoelectric currents for various metals (aluminum, nickel, and copper) were measured using the same experimental setup. The results showed consistent measurement of photoelectric current values across all metals. This study offers insights into the development of units for measuring photoelectric current and methodologies to validate their results.

Keywords: photoelectric current; photoemission effect; lunar environment; vacuum chamber



Citation: Park, S.; Chung, T.; Kim, J.; Ryu, B.; Shin, H. Design and Validation of a Photoelectric Current Measuring Unit for Lunar Daytime Simulation Chamber. *Aerospace* **2024**, *11*, 69. <https://doi.org/10.3390/aerospace11010069>

Academic Editor: Hossein Zare-Behtash

Received: 12 December 2023

Revised: 4 January 2024

Accepted: 9 January 2024

Published: 11 January 2024



Copyright: © 2024 by the authors. Licensee MDPI, Basel, Switzerland. This article is an open access article distributed under the terms and conditions of the Creative Commons Attribution (CC BY) license (<https://creativecommons.org/licenses/by/4.0/>).

1. Introduction

Any surface in space faces intense energy irradiation from sources such as soft X-rays and ultraviolet (UV) rays emitted from the upper atmosphere of the sun. This irradiation causes various problems, including charging of the surfaces of objects like satellites, spacecraft, and space debris [1,2], lunar dust charging which might lead to dust adhesion or spacesuit abrasion [3–11], material degradation [12,13], and electromagnetic interference [14,15]. A phenomenon related to these charging problems is the photoelectric current emitted from the surface of an irradiated material. The photoelectric current density on the illuminated side of the moon is the factor that most strongly influences lunar surface charging [16,17]. Given the inevitability of encountering surface charging during a space mission, it is essential to recreate environments similar to the irradiated lunar surface and assess the resultant photoelectric current.

The most direct method for simulating the charging of large structures through solar radiation is to equip a large chamber with a light source capable of inducing the photoelectric effect. Several mid–large-scale chambers with UV light sources have been designed to imitate solar radiation [18–20]. These chambers accommodate measurement units like a Faraday cup or other components to quantify the intensity of the light source, but none of these chambers have been specifically employed to measure the photoelectric current originating from a particular specimen owing to the light source in the chamber. Therefore, a unit designed specifically for measuring photoelectric currents might be useful to assess the effects of simulated solar radiation on substantial structures.

Photoelectric current measurement units (PCMUs) of diverse types have been investigated for various purposes, including the evaluation of the effect of a gold-plated surface on photoelectron emission [21,22], the measurement of the photoelectric yields of various metals [23,24], the investigation of a photoelectron sheath on a metal surface [25], and single particle dust charging by different kinds of electron source [26]. The PCMUs are typically integrated into inseparable systems along with vacuum chambers, light sources, probes, and other measurement tools. Their design has focused on quantifying the optical attributes of specific samples rather than assessing the association between the configuration of a chamber and the optical properties of materials.

The photoelectric current J_p can be calculated from the optical properties of the light source and the material. This allows estimation of the effect of solar activity on the J_p from lunar soil via assessment of the vacuum ultraviolet (VUV) irradiance spectrum of the sun and the photoelectric yield of the regolith [27]. The calculated J_p of $5.05 \mu\text{A}/\text{m}^2$ agrees well with the value of $4.5 \mu\text{A}/\text{m}^2$ obtained by Feuerbacher et al., who firstly numerically evaluated the photoelectron flux under solar irradiation [28]. The calculation method does not need any input from experimental outcomes; therefore, it possesses the potential to validate the reliability of data measured by a PCMU.

Overall, the development of PCMUs that can be used within vacuum chambers has received little research attention. However, such units would be valuable to the testing and evaluation of charging phenomena that may threaten space development and exploration missions. They could also simulate and evaluate charging environments such as those present during the lunar daytime and subsequently assess them quantitatively. In addition, research into the characteristics of photoelectric current generation based on the electrical state of objects would advance our understanding of photoelectron emission in various other scenarios.

This paper reports the design and implementation of a PCMU and presents validation calculations to assess the experimental setup. First, it introduces previously developed PCMUs and explores the motivation to design a new measurement unit. Next, the fundamental principles and configuration of the measurement system are described. The photoelectric current measurement results are then presented; they are discussed in detail in terms of control variables and compared with photoelectric currents derived analytically based on the experimental configuration. Lastly, photoelectric current measurements for various metals are also provided.

2. The Photoelectric Current Measurement Unit (PCMU)

Several studies have measured photoelectric currents from specimens. The fundamental components of the measurement units are a UV light source, the sample (photocathode), and a photoelectron capture grid (anode). Various configurations and strategies have been introduced, including using a Langmuir probe to assess photoelectron characteristics [25], a dust-dropping system combined with a Faraday cup to charge and measure the dust's charge through photoelectrons emitted from the photocathode [26], a photodiode to quantify the incidence of the UV light source, a UV collimator or an aperture to control the irradiated area [21,24], and a back collector to capture unwanted photoelectrons emitted from sources other than the photocathode specimen [21,22]. In most cases, the photoelectron collector, through which UV light passes, comprises a metal mesh grid made of materials such as nickel or platinum [21,22,26]. These metals possess a high work function (WF), making it more difficult for them to emit photoelectrons compared with other metals like aluminum.

Figure 1 shows a photograph of the PCMU and diagram of the principle of photoelectric current measurement using the PCMU. The unit incorporates an aperture, a mesh grid, a ring collector, and the sample. The aperture is used to maintain a constant area of UV radiation from the VUV lamp. By controlling the irradiated area, the photoelectric current density can be calculated from the measured photoelectric current. The sample for photoelectron emission is placed on the baseplate, below the aperture. The sample is illuminated

perpendicularly from the VUV lamp so that the emitted photoelectrons move toward the mesh grid. The nickel mesh grid electrode is positively biased to capture photoelectrons emitted from the surface of the sample; nickel was chosen for its high WF and thus low propensity to emit photoelectrons. The ring collector, positioned above the mesh grid and positively biased relative to it, captures any unwanted photoelectrons emitted from the mesh grid or any part of the experiment setup other than the sample [21,22]. Connector holders are placed around the PCMU to facilitate connections between the unit's internal components and external measurement devices. These holders can accommodate various terminal types, such as BNC and SMA connectors for coaxial cable. These terminals can be linked to the feedthrough in the chamber's wall, enabling signal communication with instruments placed outside. Provided that the length of cabling remains within a suitable range, the PCMU can be positioned at any location inside the chamber.

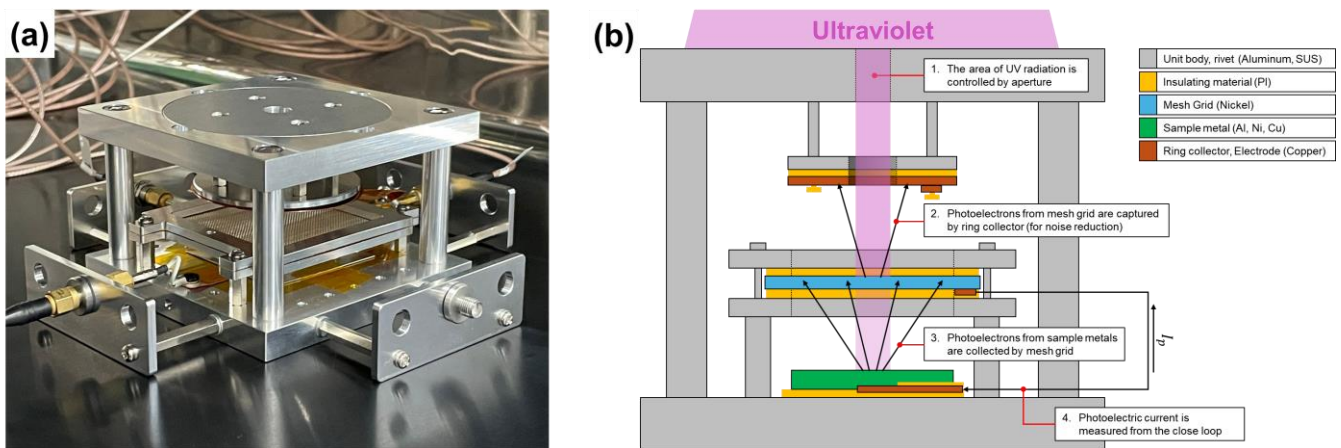


Figure 1. (a) Photograph of the photoelectric current measurement unit, and (b) diagram showing the principle of the designed measurement unit with description (not to scale).

Figure 2 shows the wiring scheme of the PCMU along with an additional measurement apparatus. The chamber's body is grounded to ensure zero potential on the walls. The electric potential of the mesh grid, denoted as ϕ_m , is manipulated through the adjustment of the voltage V_m . This voltage represents the potential difference between the mesh grid and the ground. It is essential for ϕ_m to be positive to enable the mesh grid to function as a collector of negatively charged photoelectrons. The electric potential ϕ_s of the sample is controlled by manipulating voltage V_{ms} , which equals the difference in potential between the mesh grid and the sample: $V_{ms} = \phi_m - \phi_s$. This voltage should be positive to generate an electric field between the mesh grid and the sample that will cause the mesh grid to attract photoelectrons released from the sample. Lastly, the electric potential ϕ_r of the ring collector is controlled by adjusting voltage V_{rm} , which corresponds to the potential difference between the ring collector and the mesh grid and is defined as $V_{rm} = \phi_r - \phi_m$. Similar to V_{ms} , V_{rm} must be positive to generate an electric field between the ring collector and the mesh grid that allows the ring collector to attract photoelectrons released from the mesh grid. The photoelectric current I_p arising from the stream of photoelectrons emitted from the sample's surface can be evaluated by measuring the electron flow between the mesh grid and the sample metal, assuming that the mesh grid captures all the photoelectrons emitted from the sample.

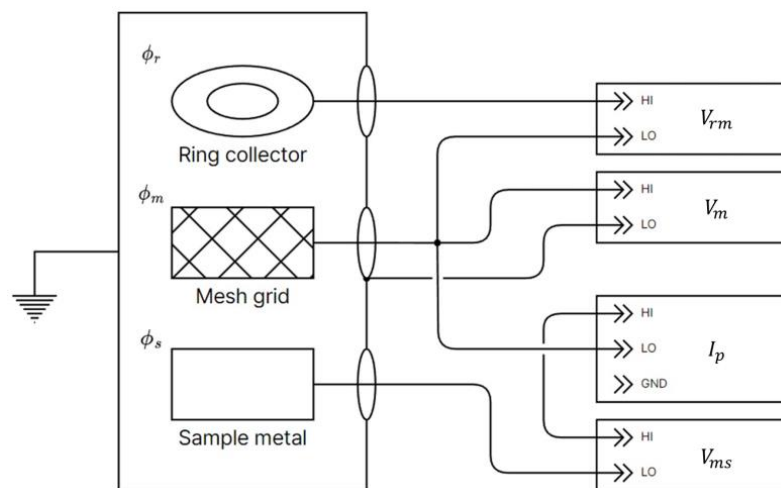


Figure 2. Wiring schematic of the photoelectric current measurement unit along with the measurement apparatus.

The photoelectric current was assessed, and I - V curves were plotted while altering the voltages V_m and V_{rm} . The voltage V_{ms} was swept from -20 to 50 V in 1 V increments while V_m and V_{rm} were held constant. Subsequently, V_m and V_{rm} were varied from 0 to 30 V in 10 V steps to obtain further I - V curves, and the converging value of I_p was identified. Lastly, I_p was divided by the illuminated area to normalize the current with respect to area and calculate the photoelectric current density J_{pm} .

3. Experimental Setup

The experiment involved the use of a specialized chamber to facilitate the surface charging of a specific material under high-vacuum conditions (Figure 3). The chamber incorporated a venturi pump, dry pump, and turbo molecular pump to achieve vacuum levels as low as 1×10^{-6} mbar. Three pressure gauges, each optimized for a specific range of vacuum levels, facilitated precise measurement of the vacuum level. A VUV lamp installed at the top of the chamber induced a positive surface charge on the experimental specimen. The chamber was connected to various devices such as a picoammeter and DC power supply through vacuum feedthroughs. Detailed specifications and information on experiments performed using the chamber have been reported elsewhere [29].

Aluminum was chosen as the sample metal for the emission of photoelectrons. High-grade aluminum was selected to mitigate the influence of impurities. The sample was 55 mm wide, 55 mm high, and 0.5 mm thick. As the photoelectric effect stems from the electrons on the material's surface, it is influenced by the surface condition of the specimen [30]. Therefore, to reveal a "fresh" surface, the aluminum sample was polished and cleaned using isopropyl alcohol before the experiment. To maximize the photoelectric effect, experiments were conducted at a pressure lower than 5×10^{-5} mbar. The nickel mesh grid featured an opening rate of 65% . The primary wavelength of the UV source was 160 nm, which is considerably shorter than 350 nm, corresponding to the WF of aluminum (3.58 eV) [31]. Experiments were repeated five times under identical conditions and average I_p . The signal baseline without UV light radiation was acquired before the measurement. By subtracting the background signal from the raw data, the converging photoelectric current values were measured. Finally, the PCMU was covered with multi-layer insulation, while keeping the aperture exposed to prevent background noise. Table 1 lists the details of the experimental setup.

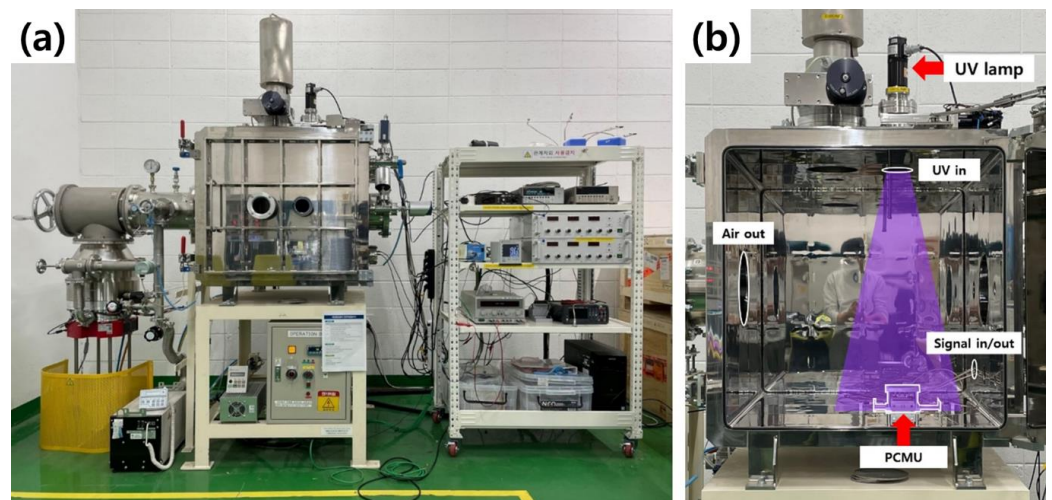


Figure 3. Photograph of the surface charging chamber: (a) the chamber with measurement equipment; (b) interior of the chamber showing placement of the photoelectric current measurement unit (PCMU), the virtual VUV radiation area illustrated in purple, and openings on the wall and PCMU outlined in white.

Table 1. Characteristic parameters of the test system.

Category	Indicator	Parameter
Settings	UV lamp	Hamamatsu L11798 (Hamamatsu Photonics K.K., Hamamatsu City, Japan)
	Sample metal	Aluminum (Nilaco Corp., Tokyo, Japan, 99.5%)
	Distance from lamp to sample	80 cm
	Mesh grid	Nickel (opening rate: 65%)
	Pressure	$<5 \times 10^{-5}$ mbar
	NPLC (Number of powerline cycles)	10
	Number of experiments/each condition	5
Instruments	Photoelectric current measurement	Keithley 6517B (Keithley Instruments, Cleveland, OH, USA)
	Potential difference between mesh and sample V_{ms} control	Keithley 6517B (Keithley Instruments, Cleveland, OH, USA)
	Mesh grid potential ϕ_m control	GPC 6030D (GW Instek, Xīnběi Shì, Taiwan)
	Potential difference between ring collector and mesh V_{rm} control	GPC 6030D (GW Instek, Xīnběi Shì, Taiwan)
	Data acquisition (DAQ)	NI-9205 (National Instruments Corporation, Austin, TX, USA)

4. Measurement

Figure 4 shows the result of I - V curve analysis and statistical assessment. From the sixteen measurements, certain characteristics are observed.

- In the I - V curve, as V_{ms} changed from negative to positive, the current I_p followed the same polarity transition.
- As V_{ms} crossed 0 V, the magnitude of the current rapidly increased.
- As V_{ms} reached the value of ϕ_m , the current slightly increased.
- After V_{ms} exceeded ~ 40 V, the I_p tended to converge to a certain value.

The effect of V_{rm} was negligible across all ϕ_m conditions, whereas variation of ϕ_m appeared to influence the shape of the curve with increasing V_{ms} . Further discussion on the changes in I_p are provided later in this section.

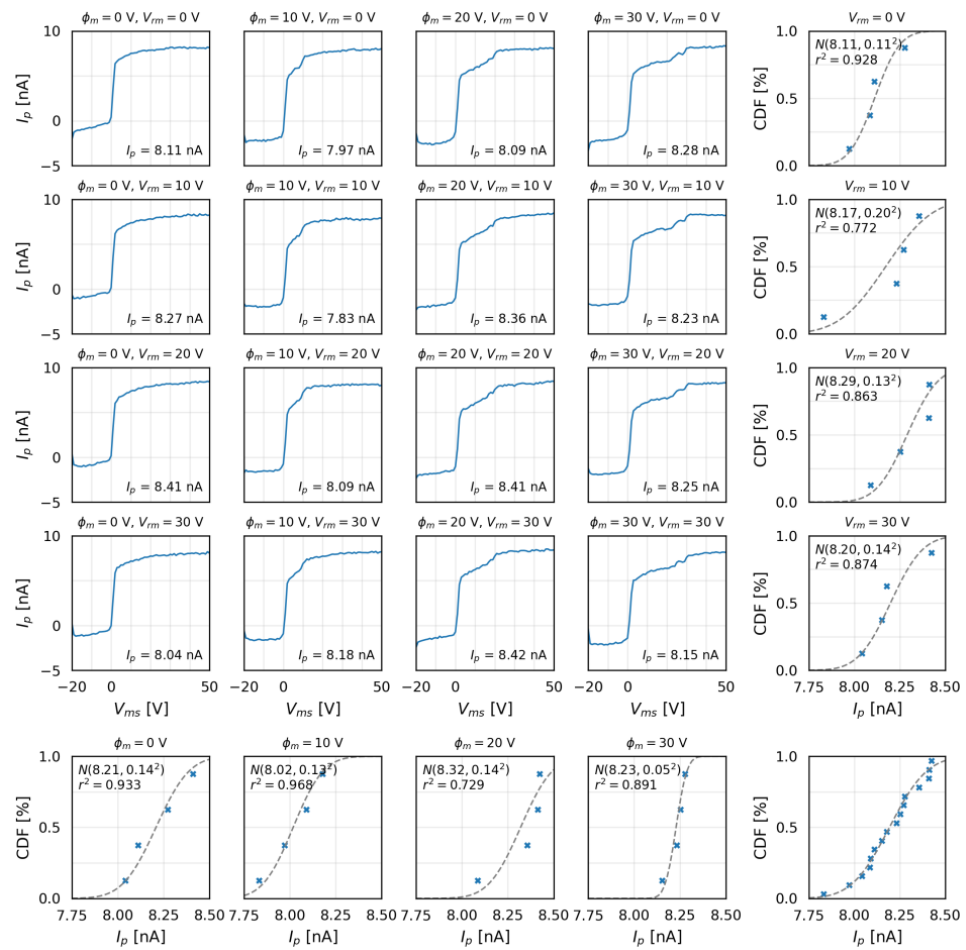


Figure 4. I – V curves and calculations of statistical parameters for converging I_p values under various conditions. The I – V curves plot photoelectric current while sweeping V_{ms} under various constant values of mesh grid potential ϕ_m and potential difference between ring collector and mesh grid V_{rm} . The lower right corner of each I – V plot is labeled with the converged photoelectric current value. To the right of and below the I – V curves are cumulative normal distribution curves fitted to the experimental data measured at constant V_{rm} and ϕ_m , respectively. The crosses in these plots indicate the converged I_p values for each set of experimental conditions, and the gray dashed lines are fitted cumulative normal distribution curves. Each fitted normal distribution is labeled as $N(\bar{X}, s^2)$ in the upper left corner of each graph, where \bar{X} and s represent the mean and the standard deviation, respectively.

4.1. Consistency of Measured Values

The converged values of I_p under each set of experimental conditions are grouped by constant ϕ_m and constant V_{rm} , and each group is then fitted to a normal distribution. These fitted distributions are presented to the right of and below the measured I – V plots. Those to the right represent the fitted distribution based on constant V_{rm} , and those below represent the distributions fitted for results measured at constant ϕ_m . To quantify the converged values of I_p , the characteristic parameters of each normal distribution (i.e., mean and standard deviation) were calculated. These were then used to derive coefficients of variance (CV) for each analysis condition to quantitatively assess the measurement error, as follows [32,33]:

$$CV = s/\bar{X}. \tag{1}$$

The CV did not exceed 0.03 under any set of measurement conditions, indicating consistent measurements. Combining all 16 measured values and fitting them into a

normal distribution yielded the plot in the lower right corner of Figure 4. The CV remained below 0.02, showing that the measurement unit could achieve reasonable precision.

4.2. Effects of ϕ_m and V_{rm} on I_p

To quantify the effect on I_p of parameters ϕ_m and V_{rm} , which affected on the shapes of the I - V curves, similarity among the plots was investigated. To quantify the similarity between the I - V curves, we calculated the Euclidean distance (ED), a measure commonly used for assessing similarity between two time-series datasets [34]. A low ED value indicates great similarity between the two graphs. The ED between two curves with data series u and v is defined as follows:

$$ED = \sqrt{\sum_{i=1}^n (u_i - v_i)^2}, \tag{2}$$

where u_i and v_i are the data of the time series u and v , respectively. In this experiment, u and v are the I - V curves with specific experimental conditions of ϕ_m and V_{rm} . Each condition of constant ϕ_m or V_{rm} yielded six EDs. Figure 5 shows the EDs between each pair of measured datasets. The EDs between datasets with constant V_{rm} and differing ϕ_m were greater than those between pairs with constant ϕ_m and differing V_{rm} . In other words, ϕ_m more greatly affected I_p than did V_{rm} . Increasing the difference between ϕ_m values (at constant V_{rm}) led to increasing EDs; however, no such relationship was found when increasing V_{rm} (at constant ϕ_m).

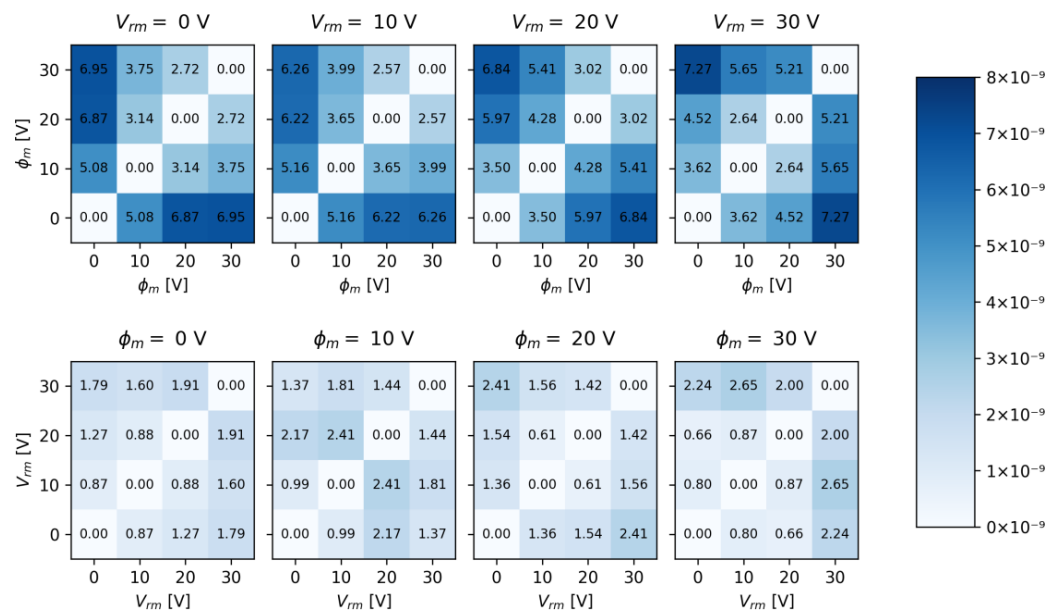


Figure 5. Euclidean distance heat maps for constant V_{rm} (upper row) and ϕ_m (lower row). Each numerical value within the heat maps should be multiplied by 10^{-9} (e.g., 2.24 represents an ED of 2.24×10^{-9}).

4.3. Variation of I_p with Changing V_{ms}

The variation of I_p with changes in V_{ms} can be considered from two perspectives. First, V_{ms} influences the electric field between the sample (where photoelectrons are generated) and the mesh grid (which captures them). A negative V_{ms} means the potential of the sample is greater than that of the mesh grid, resulting in a positive value for the electric field in the z -direction (i.e., normal to the sample, toward the mesh grid). Therefore, the photoelectrons from the sample experience a force in the negative z -direction, which prevents most of them from being able to escape, and they return to the sample. Any photoelectrons generated on the mesh grid are also attracted toward the sample. The flow of electrons in the reverse

direction creates a backward electron motion in the designed circuit, which leads to negative I_p values (Figure 6a). At $V_{ms} = 0$, there is no electric field between the mesh grid and the sample, so there is no electron flow between the two electrodes, and thus nearly no electric current (Figure 6b). When V_{ms} is positive, the potential of the sample becomes smaller than that of the mesh grid, resulting in the electric field being negative in the z-direction. Consequently, electrons are attracted toward the mesh grid, moving in the z-direction from the sample toward the grid (Figure 6c). As a result, the photoelectrons generated in the sample are captured by the mesh grid, and this movement of electrons is recorded as positive I_p values.

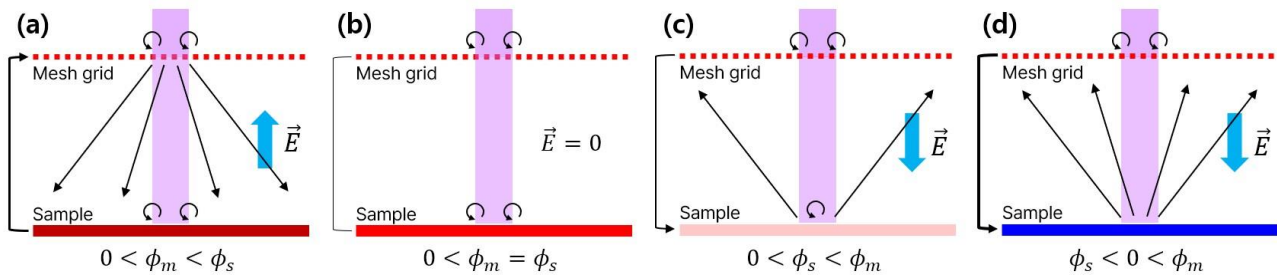


Figure 6. Graphical representation of four cases of electron movement between the mesh grid (dashed red line) and sample metal (bottom thick line) in the PCMU (front view): (a) $0 < \phi_m < \phi_s$, (b) $0 < \phi_m = \phi_s$, (c) $0 < \phi_s < \phi_m$, and (d) $\phi_s < 0 < \phi_m$. The purple area represents ultraviolet radiation from the top of the PCMU. The large blue arrow indicates the direction of the electric field. Thin black arrows show the movement of electrons; a circular arrow represents photoelectrons “returning”, owing to the emitting surface being positively charged.

The next consideration is that of the electric potentials of the sample and mesh grid. As electrons are attracted to positively charged surfaces, any metal sample with positive potential that emits photoelectrons will immediately attract them back to the sample. This phenomenon is similar to the surface charging mechanisms observed during the lunar daytime: incidents of high-energy solar photons (e.g., soft X-ray and UV) collide with electrically floating surfaces, resulting in the emission of photoelectrons and the subsequent development of a positive surface charge. As the electrons leave the lunar surface, the potential of the lunar surface ϕ_0 increases. However, as soon as ϕ_0 becomes positively charged, the ejected photoelectrons are attracted back toward the lunar surface, initiating their return. Overall, the initial phase has more photoelectrons leaving than returning, causing ϕ_0 to rise; when ϕ_0 reaches a certain threshold ϕ_s , the surface draws back as many photoelectrons as those leaving, and the surface charge ϕ_0 stabilizes. ϕ_s is known to be approximately +10 V [35,36]. The returned electrons interacting with the surface form a layer near the surface that acts as a sheath to prevent further photoelectrons from leaving [37]. A similar phenomenon occurred on the surface of the sample metal within the PCMU: when the surface of the sample was positively charged, a photoelectric sheath was generated, which prevented photoelectrons from escaping. The generated electrons then cannot reach the mesh grid, even in the presence of an external electric field, resulting in the non-measurement of photoelectric current. When ϕ_m becomes greater than ϕ_s , and ϕ_s becomes negative, the surface starts to repel photoelectrons. The repelled photoelectrons are drawn toward the mesh grid, which holds a positive potential, resulting in the convergence of the photoelectric current to a stable value (Figure 6d).

4.4. Photoelectric Current Density Calculation and Method Validation

To normalize the photoelectric current and characterize the photoelectric effect, the measured current should be expressed in terms of current density. To calculate the current density from the measured photoelectric current of 8.19 nA, the current should be divided by the area from which it originated. The area is determined by multiplying the aperture area of the PCMU and the opening rate of the mesh grid through which the UV

passes. These values are $78.54 \times 10^{-9} \text{ m}^2$ and 0.65, respectively, giving a current density of $160 \times 10^{-6} \text{ A/m}^2$. This value is labeled J_{pm} to represent it being the measured photoelectric current density J_p from the PCMU.

To validate the value of J_{pm} , the expected J_p is calculated for the given experimental conditions. This calculated photoelectric current density is denoted as J_{pc} ; the calculation is based on previous research [19,21]. The calculation requires information about the irradiance spectrum $F(\lambda)$ of the light source and the photoelectric yield $Y(\lambda)$ of the sample. $F(\lambda)$ is a measure of the radiant flux received per unit area at different wavelengths of electromagnetic radiation. From the spectrum $F(\lambda)$, the photon emission spectrum $S(\lambda)$ can be calculated as follows [38]:

$$S(\lambda) = F(\lambda)/E(\lambda) = F(\lambda) \cdot \frac{\lambda}{hc}, \quad (3)$$

where $E(\lambda)$ is the energy equivalent to a photon with wavelength λ , h is Planck's constant, and c is the speed of light. The photon emission spectrum describes the number of photons emitted from the light source at each specific wavelength, measured in [photon/cm²·s·nm]. Parameter $Y(\lambda)$ is the probability of photoelectron generation from the sample's surface per incident photon, which is defined as a function of wavelength; its units are [electron/photon] [39].

The first step to calculate J_{pc} from $S(\lambda)$ and $Y(\lambda)$ is to multiply $S(\lambda)$ and $Y(\lambda)$ with respect to λ . This gives a function representing the number of photoelectrons emitted per unit area from the sample when illuminated at a given wavelength. The function is the differential photoelectron flux and is denoted as $H(\lambda)$. Integrating $H(\lambda)$ over the wavelength range of the light source gives the total number of photoelectrons emitted per unit area. Multiplying the result by the elementary charge e gives the charge carried by the photoelectrons per unit area, which corresponds to the photoelectric current density J_p . This can be expressed as follows [27]:

$$J_p = e \int_{\lambda_{low.}}^{\lambda_{up.}} H(\lambda) d\lambda = e \int_{\lambda_{low.}}^{\lambda_{up.}} Y(\lambda) S(\lambda) d\lambda, \quad (4)$$

where $\lambda_{up.}$ represents the upper limit of the wavelength range of the light source, and $\lambda_{low.}$ corresponds to the lower limit of the wavelength range of the light source, or possibly the wavelength corresponding to the WF of the specimen if that is smaller than the upper limit of the wavelength range of the light source.

The irradiance spectrum in Figure 7a was provided by the manufacturer of the UV light source. The emission ranged approximately from 75 to 280 nm, with the highest intensity in a narrow band around 160 nm. The photoelectric yield of aluminum shown in Figure 7b is adopted from previous work [40]. The wavelength range for Al to show the photoelectric electric effect overlaps with the photon emission spectrum of the UV light source, so photoelectron emissions are expected here. Figure 7b excludes yields for wavelengths below 50 nm; however, these wavelengths do not coincide with the emission range of the light source, so their absence is inconsequential here.

The cumulative plot of calculated J_{pc} in Figure 8 shows a steep increase from around 75 nm to approximately 130 nm and then a gradual increase to around 160 nm, above which J_{pc} no longer increases. This observation can be attributed to the sharp decrease in the photoelectric yield for wavelengths above 160 nm. These results give a calculated value of J_{pc} of approximately $169 \times 10^{-6} \text{ A/m}^2$, which is similar to the measured value of $J_{pm} = 160 \times 10^{-6} \text{ A/m}^2$. The observed error, based on the average value as a reference, was approximately 5.5%, which is reasonably acceptable.

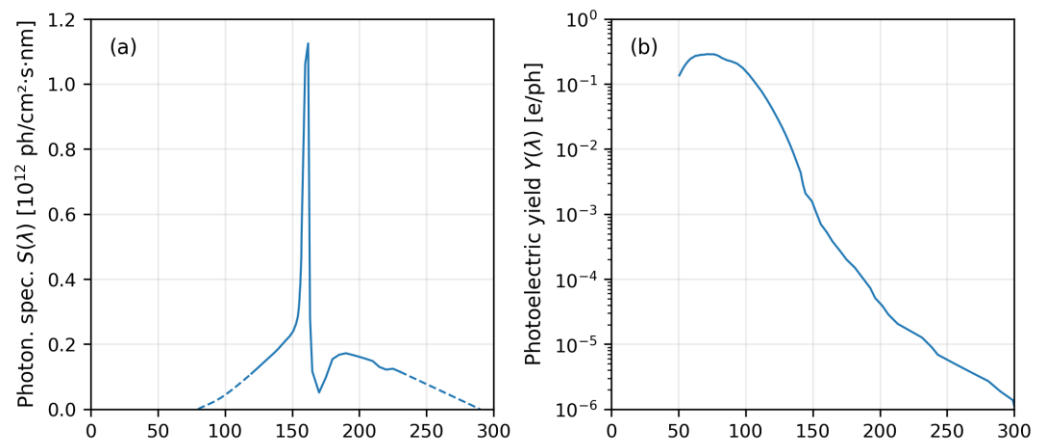


Figure 7. Optical properties for calculating photoelectric current density: (a) photon emission spectrum at a distance of 50 cm from the light source, and (b) photoelectric yield of aluminum.

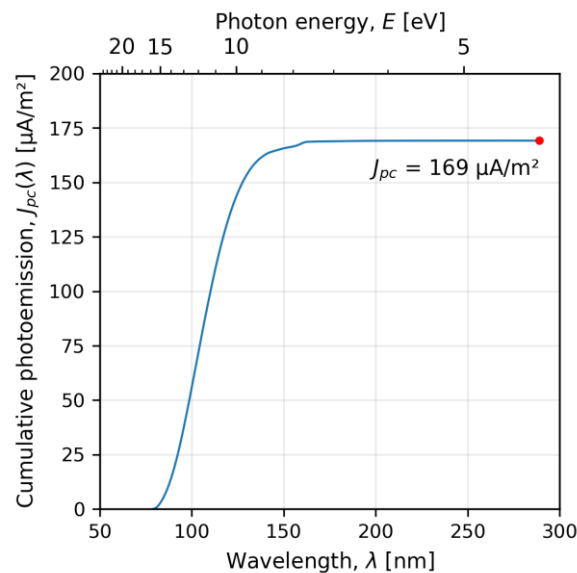


Figure 8. Cumulative photoelectric current calculated using data from Figure 7 for the UV light source and the aluminum sample used in the experiments.

4.5. Comparison of I_p Measurements for Different Metals

Using the PCMU, I_p values were evaluated for three metals (aluminum, nickel, and copper) with the same FCC crystal structure. The metals were prepared using the polishing and drying procedures described in Section 3. Ten repeated measurements were conducted for each of the 16 experimental conditions, resulting in a convergent dataset for each condition. The distributions of these values (visualized as box plots in Figure 9) yielded parameters for the normal distributions fitted to the measured I_p values of the metals (Table 2). The measurement results showed that the CV of nickel's I_p was higher than that of aluminum and copper. Possibly due to aluminum and copper having lower surface hardness than nickel [41], which resulted in their effective polishing and reduced surface contamination; lower variance data were obtained. Despite nickel having the highest CV for its measured I_p , the value remained below 0.04, indicating a high level of precision in the measurement. Overall, the presented results demonstrate the PCMU to be a capable instrument for efficiently measuring the photocurrent generated from metals; therefore, it can enable effective reevaluation of the photoemission characteristics of these materials.

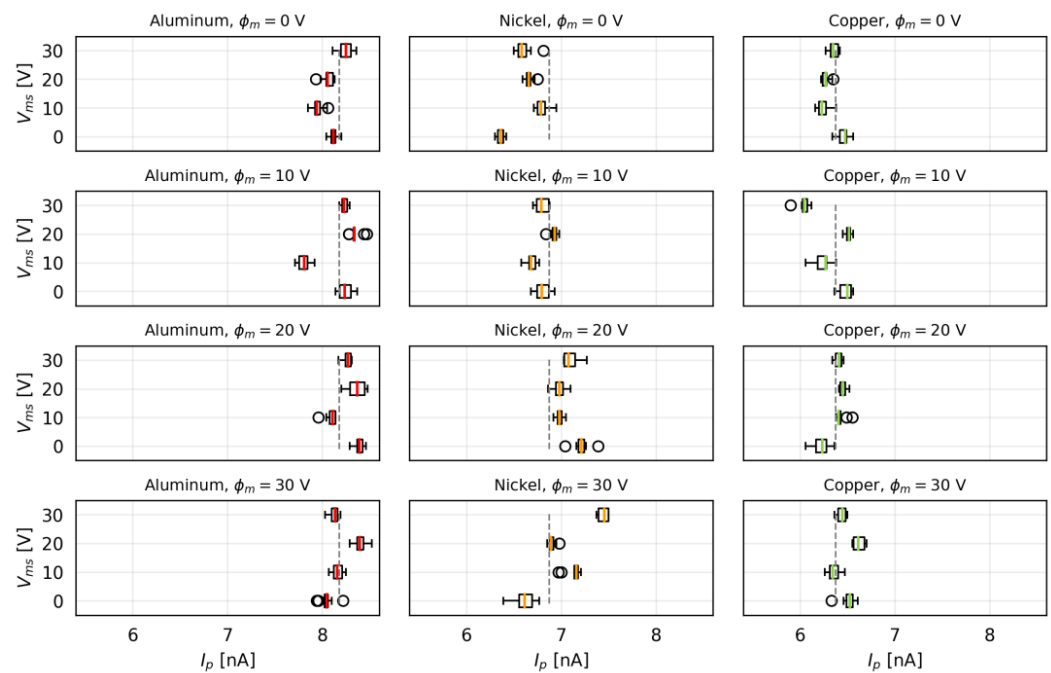


Figure 9. Comparison of photoelectric currents measured for three metals: aluminum, nickel, and copper. Box plots show the distributions of values for each experimental condition (given at the top of each plot). Dashed lines indicate the mean photoelectric current for each metal.

Table 2. Normal distribution parameters fitted to distributions of measured I_p values for various metals and the coefficient variations calculated from \bar{X} and s .

Metals	Mean	Standard Deviation	Coefficient of Variation
Aluminum	8.17	0.172	0.0211
Nickel	6.88	0.269	0.0391
Copper	6.38	0.152	0.0238

5. Conclusions and Future Work

This study introduced a PCMU for a chamber simulating the lunar daytime. The measurement unit comprised a mesh grid, a photocathode sample, and a noise-capturing ring collector. The unit was designed to capture photoelectrons emitted from a sample irradiated by UV light within a vacuum chamber. Data for I - V curves were gathered by measuring the photoelectric current I_p while sweeping the potential difference V_{rm} between the mesh grid and sample. Despite the influence of mesh grid potential ϕ_m on the I - V curve profile, the PCMU produced I_p with reasonable levels of precision: the coefficient of variance was less than 0.03. The photoelectric current density derived from measurements of an aluminum sample was $160 \times 10^{-6} \text{ A/m}^2$. Comparison of this value with the current density calculated for the experimental setup ($169 \times 10^{-6} \text{ A/m}^2$) showed that the measured results were reasonably acceptable, with an error of less than 5.5%. Lastly, photoelectric currents generated from three different metals (aluminum, nickel, and copper) were measured and CV for photoelectric currents from these metals was consistently below 0.04, indicating a commendable precision in the measurement. Consequently, the PCMU designed in this study is suitable for assessing the photoelectric effect occurring within a vacuum chamber. This study provides information for the development of such measurement units and methods for their validation.

The unit is designed for measuring photoelectrons emitted from metals with adjustable electric potential. However, to deal with photoelectrons generated from insulators such as lunar soil or its simulants, the current measurement design would require modification. Furthermore, to improve the simulation of lunar daytime conditions, the chamber would

need to replicate solar wind plasma with a low density of ions and electrons. Given these considerations, our future work will develop a PCMU for use within a dirty thermal vacuum chamber at the Korea Institute of Civil Engineering and Building Technology and establish a validation methodology for test environments simulating surface charging environments for in situ resources utilization test beds during the lunar day and night.

Author Contributions: Writing—original draft, S.P.; Supervision, T.C. and J.K.; Resources, B.R.; Project administration, H.S. All authors have read and agreed to the published version of the manuscript.

Funding: This research was funded by the Department of Future & Smart Construction Research of the Korea Institute of Civil Engineering and Building Technology, grant number 20230081-001.

Data Availability Statement: The data that support the findings of this study are available from the corresponding author, Seungsoo Park (ssglenpark@kict.re.kr), upon reasonable request.

Conflicts of Interest: Author Jihyun Kim was employed by the company Wonik IPS Co., Ltd. The remaining authors declare that the research was conducted in the absence of any commercial or financial relationships that could be construed as a potential conflict of interest.

Abbreviation

Definitions of variables and acronyms.

Symbol	Definition
c	The speed of light (299,792,458 m/s)
e	Elementary charge (2.9×10^{-19} C)
$E(\lambda)$	Energy equivalent to a photon with wavelength λ , $E(\lambda) = hc/\lambda$
$F(\lambda)$	Irradiance spectrum of light source
$H(\lambda)$	Differential photoelectron flux, $H(\lambda) = S(\lambda)Y(\lambda)$
h	Planck's constant (6.626×10^{-34} J·s)
I_p	Photoelectron current
J	Generic current density
J_p	Photoelectron current density
J_{pc}	Photoelectron current density calculated from experimental setup
J_{pm}	Photoelectron current density calculated from measured I_p using PCMU
$N(\bar{X}, s^2)$	Normal distribution with mean \bar{X} and standard deviation s
s	Standard deviation of the samples
$S(\lambda)$	Photon emission spectrum of light source
V	Electric potential difference
V_m	Electric potential difference between mesh grid and ground, $V_m = \phi_m$
V_{ms}	Electric potential difference between mesh grid and sample metal, $V_{ms} = \phi_m - \phi_s$
V_{rm}	Electric potential difference between ring collector and mesh grid, $V_{rm} = \phi_r - \phi_m$
\bar{X}	Mean of the samples
$Y(\lambda)$	Photoelectric yield of material
λ	Wavelength
λ_{low}	Lower limit of the wavelength range of light source
λ_{up}	Upper limit of the wavelength range of light source
ϕ	Electric potential with respect to electric ground
ϕ_0	Electric potential of lunar surface with respect to electric ground
ϕ_m	Electric potential of mesh grid with respect to electric ground
ϕ_s	Electric potential of sample metal with respect to electric ground
ϕ_S	Electric potential of lunar surface electrostatically steady-state condition
ϕ_r	Electric potential of ring collector with respect to electric ground

Acronym	Definition
CDF	Cumulative distribution function
CV	Coefficient of variation, $CV = \sigma/\mu$
ED	Euclidean distance
DTVC	Dirty thermal vacuum chamber
KICT	Korea Institute of Civil Engineering and Building Technology
PCMU	Photoelectric current measuring unit
SED	The sum of Euclidean distances
UV	Ultraviolet (10–400 nm)
VUV	Vacuum ultraviolet (10–200 nm)
WF	Work function

References

- Ganushkina, N.Y.; Swiger, B.; Dubyagin, S.; Matéo-Vélez, J.-C.; Liemohn, M.W.; Sicard, A.; Payan, D. Worst-Case Severe Environments for Surface Charging Observed at LANL Satellites as Dependent on Solar Wind and Geomagnetic Conditions. *Space Weather* **2021**, *19*, e2021SW002732. [\[CrossRef\]](#)
- Paul, S.N.; Frueh, C. Space Debris Charging and Its Effect on Orbit Evolution. In Proceedings of the AIAA/AAS Astrodynamics Specialist Conference, Long Beach, CA, USA, 13–16 September 2016; pp. 1–31.
- Wang, H.; Phillips, J.R.; Dove, A.R.; Elgohary, T.A. Investigating Particle-Particle Electrostatic Effects on Charged Lunar Dust Transport via Discrete Element Modeling. *Adv. Space Res.* **2022**, *70*, 3231–3248. [\[CrossRef\]](#)
- Yang, K.; Feng, W.; Xu, L.; Liu, X. Review of Research on Lunar Dust Dynamics. *Astrophys. Space Sci.* **2022**, *367*, 67. [\[CrossRef\]](#)
- Barker, D.C.; Olivas, A.; Farr, B.; Wang, X.; Buhler, C.R.; Wilson, J.; Mai, J. Adhesion of Lunar Simulant Dust to Materials under Simulated Lunar Environment Conditions. *Acta Astronaut.* **2022**, *199*, 25–36. [\[CrossRef\]](#)
- Mishra, S.K.; Misra, S. Charging and Dynamics of Dust Particles in Lunar Photoelectron Sheath. *Phys. Plasmas* **2019**, *26*, 053703. [\[CrossRef\]](#)
- Mishra, S.K.; Bhardwaj, A. Photoelectron Sheath on Lunar Sunlit Regolith and Dust Levitation. *Astrophys. J.* **2019**, *884*, 5. [\[CrossRef\]](#)
- Wang, X.; Schwan, J.; Hsu, H.-W.; Grün, E.; Horányi, M. Dust Charging and Transport on Airless Planetary Bodies. *Geophys. Res. Lett.* **2016**, *43*, 6103–6110. [\[CrossRef\]](#)
- Ding, N.; Wang, J. Polansky Measurement of Dust Charging on a Lunar Regolith Simulant Surface. *IEEE Trans. Plasma Sci.* **2013**, *41*, 3498–3504. [\[CrossRef\]](#)
- Tankosic, D.; Abbas, M.M. Laboratory Studies of Charging Properties of Dust Grains in Astrophysical/Planetary Environments. *J. Phys. Conf. Ser.* **2012**, *399*, 012024. [\[CrossRef\]](#)
- Wells, I.; Bussey, J.; Swets, N.; Leachman, J. Lunar Dust Removal and Material Degradation from Liquid Nitrogen Sprays. *Acta Astronaut.* **2023**, *206*, 30–42. [\[CrossRef\]](#)
- Bitetti, G.; Marchetti, M.; Mileti, S.; Valente, F.; Scaglione, S. Degradation of the Surfaces Exposed to the Space Environment. *Acta Astronaut.* **2007**, *60*, 166–174. [\[CrossRef\]](#)
- Dever, J.; Banks, B.; de Groh, K.; Miller, S. Degradation of Spacecraft Materials. In *Handbook of Environmental Degradation of Materials*; Kutz, M., Ed.; William Andrew Publishing: Norwich, NY, USA, 2005; pp. 465–501, ISBN 978-0-8155-1500-5.
- Payan, D. Payan Electrostatic Behaviour of Materials in a Charging Space Environment. In Proceedings of the 2004 IEEE International Conference on Solid Dielectrics, 2004. ICSD 2004, Toulouse, France, 5–9 July 2004; Volume 2, pp. 917–927.
- McCollum, M.; Kim, L.; Lowe, C. Electromagnetic Compatibility Considerations for International Space Station Payload Developers. In Proceedings of the 2020 IEEE Aerospace Conference, Big Sky, MT, USA, 7–14 March 2020; pp. 1–9.
- Stubbs, T.J.; Halekas, J.S.; Farrell, W.M.; Vondrak, R.R. *Lunar Surface Charging: A Global Perspective Using Lunar Prospector Data*; Krueger, H., Graps, A., Eds.; University of California: Berkeley, CA, USA, 2007; Volume 643, pp. 181–184.
- Stubbs, T.J.; Farrell, W.M.; Halekas, J.S.; Burchill, J.K.; Collier, M.R.; Zimmerman, M.I.; Vondrak, R.R.; Delory, G.T.; Pfaff, R.F. Dependence of Lunar Surface Charging on Solar Wind Plasma Conditions and Solar Irradiation. *Planet. Space Sci.* **2014**, *90*, 10–27. [\[CrossRef\]](#)
- Kruzelecky, R.V.; Murzionak, P.; Burbulea, P.; Mena, M.; Sinclair, I.; Schinn, G.; Cloutis, E.; Communications, M. Dusty Thermal Vacuum (DTVAC) Facility Payloads Operations under Simulated Lunar Environment. In Proceedings of the Earth and Space 2021, Virtually, 19–23 April 2021.
- Vakkada Ramachandran, A.; Nazarious, M.I.; Mathanlal, T.; Zorzano, M.-P.; Martín-Torres, J. Space Environmental Chamber for Planetary Studies. *Sensors* **2020**, *20*, 3996. [\[CrossRef\]](#) [\[PubMed\]](#)
- Craven, P.; Vaughn, J.; Schneider, T.; Norwood, J.; Abbas, M.; Alexander, R. MSFC Lunar Environments Test System (LETS) System Development. In Proceedings of the Third Lunar Regolith Simulant Workshop, Huntsville, AL, USA, 17–20 March 2009.
- Wass, P.J.; Hollington, D.; Sumner, T.J.; Yang, F.; Pfeil, M. Effective Decrease of Photoelectric Emission Threshold from Gold Plated Surfaces. *Rev. Sci. Instrum.* **2019**, *90*, 064501. [\[CrossRef\]](#) [\[PubMed\]](#)

22. Hechenblaikner, G.; Ziegler, T.; Biswas, I.; Seibel, C.; Schulze, M.; Brandt, N.; Schöll, A.; Bergner, P.; Reinert, F.T. Energy Distribution and Quantum Yield for Photoemission from Air-Contaminated Gold Surfaces under Ultraviolet Illumination Close to the Threshold. *J. Appl. Phys.* **2012**, *111*, 124914. [[CrossRef](#)]
23. Cairns, R.B.; Samson, J.A.R. *Photoelectric Yields of Metals in the Vacuum Ultraviolet*; GCA Corporation: San Francisco, CA, USA, 1966.
24. Chen, Y.; Yang, Y.; Huang, G.; Li, H.; Li, C.; Wang, S.; Cheng, Y. Development of Photoelectron Emission Yield Measurement System for Metal Materials. In Proceedings of the 2020 International Conference on Sensing, Measurement & Data Analytics in the era of Artificial Intelligence (ICSMD), Xi'an, China, 15–17 October 2020; pp. 148–151.
25. Dove, A.; Horányi, M.; Wang, X.; Piquette, M.; Poppe, A.R.; Robertson, S. Experimental Study of a Photoelectron Sheath. *Phys. Plasmas* **2012**, *19*, 043502. [[CrossRef](#)]
26. Sickafoose, A.A.; Colwell, J.E.; Horányi, M.; Robertson, S. Experimental Investigations on Photoelectric and Triboelectric Charging of Dust. *J. Geophys. Res. Space Phys.* **2001**, *106*, 8343–8356. [[CrossRef](#)]
27. Sternovsky, Z.; Chamberlin, P.; Horányi, M.; Robertson, S.; Wang, X. Variability of the Lunar Photoelectron Sheath and Dust Mobility Due to Solar Activity. *J. Geophys. Res. Space Phys.* **2008**, *113*, 1–4. [[CrossRef](#)]
28. Feuerbacher, B.; Anderegg, M.; Fitton, B.; Laude, L.D.; Willis, R.F.; Grard, R.J.L. Photoemission from Lunar Surface Fines and the Lunar Photoelectron Sheath. In Proceedings of the Third Lunar Science Conference, Houston, TX, USA, 10–13 January 1972.
29. Hong, G.-W.; Kim, J.; Shin, H.-S.; Chung, T. Development of Lunar Surface Charging Environment Simulation Chamber. *Trans. Korean Soc. Mech. Eng.* **2021**, *45*, 377–387. [[CrossRef](#)]
30. Dove, A.; Horányi, M.; Robertson, S.; Wang, X. Laboratory Investigation of the Effect of Surface Roughness on Photoemission from Surfaces in Space. *Planet. Space Sci.* **2018**, *156*, 92–95. [[CrossRef](#)]
31. Baikie, I.D.; Grain, A.C.; Sutherland, J.; Law, J. Ambient Pressure Photoemission Spectroscopy of Metal Surfaces. *Appl. Surf. Sci.* **2014**, *323*, 45–53. [[CrossRef](#)]
32. Shechtman, O. The Coefficient of Variation as an Index of Measurement Reliability. In *Methods of Clinical Epidemiology*; Doi, S.A.R., Williams, G.M., Eds.; Springer: Berlin/Heidelberg, Germany, 2013; pp. 39–49, ISBN 978-3-642-37131-8.
33. Jalilibal, Z.; Amiri, A.; Castagliola, P.; Khoo, M.B.C. Monitoring the Coefficient of Variation: A Literature Review. *Comput. Ind. Eng.* **2021**, *161*, 107600. [[CrossRef](#)]
34. Cheng, L.; Zhu, P.; Sun, W.; Han, Z.; Tang, K.; Cui, X. Time Series Classification by Euclidean Distance-Based Visibility Graph. *Phys. A Stat. Mech. Appl.* **2023**, *625*, 129010. [[CrossRef](#)]
35. Colwell, J.E.; Batiste, S.; Horányi, M.; Robertson, S.; Sture, S. Lunar Surface: Dust Dynamics and Regolith Mechanics. *Rev. Geophys.* **2007**, *45*. [[CrossRef](#)]
36. Freeman, J.W.; Ibrahim, M. Lunar Electric Fields, Surface Potential and Associated Plasma Sheaths. *Moon* **1975**, *14*, 103–114. [[CrossRef](#)]
37. Sodha, M.S.; Mishra, S.K. Lunar Photoelectron Sheath and Levitation of Dust. *Phys. Plasmas* **2014**, *21*, 093704. [[CrossRef](#)]
38. Baker, D.J. Rayleigh, the Unit for Light Radiance. *Appl. Opt.* **1974**, *13*, 2160–2163. [[CrossRef](#)] [[PubMed](#)]
39. Abbas, M.M.; Tankosic, D.; Craven, P.D.; Hoover, R.B.; Taylor, L.A.; Spann, J.F.; Leclair, A.; West, E.A. Measurements of Photoelectric Yields of Individual Lunar Dust Grains. In Proceedings of the Dust in Planetary Systems, Kauai, HI, USA, 26–30 September 2005.
40. Feuerbacher, B.; Fitton, B. Experimental Investigation of Photoemission from Satellite Surface Materials. *J. Appl. Phys.* **1972**, *43*, 1563–1572. [[CrossRef](#)]
41. Angus, H.T. The Significance of Hardness. *Wear* **1979**, *54*, 33–78. [[CrossRef](#)]

Disclaimer/Publisher's Note: The statements, opinions and data contained in all publications are solely those of the individual author(s) and contributor(s) and not of MDPI and/or the editor(s). MDPI and/or the editor(s) disclaim responsibility for any injury to people or property resulting from any ideas, methods, instructions or products referred to in the content.